# CHAPTER 3

# RESULTS AND DISCUSSIONS

Results and discussions are explained in three parts. In the first part, the results of characterization and structure analysis of nonfunctionalized and functionalized MWCNTs support are displayed. The second part, the electrochemical and electrocatalytic characteristics of the electrooxidation of small organic molecules on PtAu-MWCNTs prepared by THPC reduction method and electrodeposition method are illustrated. Then, the morphology and composition of the PtAu-MWCNTs are also stated by TEM and EDX. Finally, the morphology and composition of PdPt-MWCNTs are described by TEM, EDX and XRD. Then, the results of characterization and electrochemical measurement of PdPt-MWCNTs prepared by THPC and sodium L-ascorbate reduction methods are explained.

## 3.1 Characterization and structure analysis of nonfunctionalized and functionalized MWCNTs

FTIR spectra were obtained by passing infrared radiation through a thin sample of compound and measuring energies of the applied infrared radiation transmitted by the sample. Fourier transformations of these signals are expressed in term of wavenumbers ($cm^{-1}$) against transmittance. Figure 3.1 shows the FTIR spectra of nonfunctionalized MWCNTs and functionalized MWCNTs. The MWCNTs exhibit a strong absorbance and often are unable to be distinguished from the background noise because of their black character [49]. Therefore, a very low concentration of the

MWCNTs was used in a KBr powder. The IR spectrum of functionalized MWCNTs shows four major peaks located at 3516-3867, 2850-2920, 1643-1700, 1523-1550, 1207 and 500-1000 $cm^{-1}$. The peak at 500-1000 $cm^{-1}$ corresponds to hexagonal carbon [70]. According to the work of N. A. Buang et al. [53], the peak at 1523-1550 $cm^{-1}$ in both FTIR spectra of nonfunctionalized MWCNTs and functionalized MWCNTs corresponds to the carbon nanotube backbone stretching. The peak at 1643-1700 $cm^{-1}$ and 1207 $cm^{-1}$ can be assigned to the C=O and C−O stretching vibration from carboxyl groups (O=C−OH), respectively. The weak peaks at 2850-2920 $cm^{-1}$ correspond to the C−H stretching vibration. The strong peaks corresponding to strong absorption at 3516-3867 $cm^{-1}$ in FTIR spectra of functionalized MWCNTs and a broad peak at 3452-3516 $cm^{-1}$ in FTIR spectra of nonfunctionalized MWCNTs can be ascribed to O−H stretching vibration in the carboxylic acid group [71].

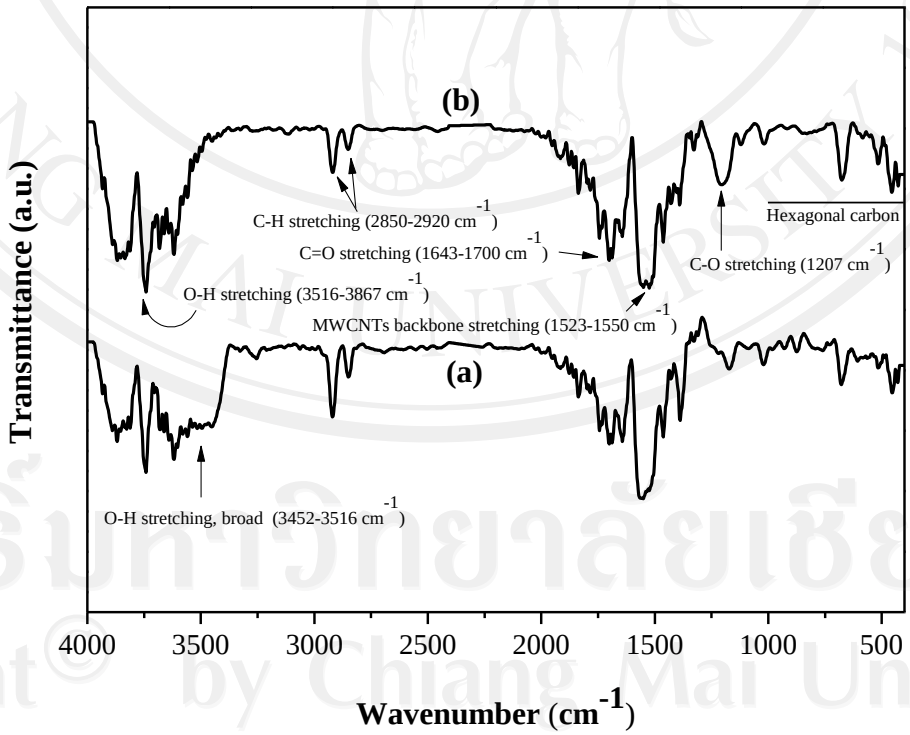


**Figure 3.1** FTIR spectra for (a) nonfunctionalized MWCNTs and (b) functionalized MWCNTs.

### 3.2 Transmission electron microscopy (TEM) and Energy-dispersive X-ray spectroscopy (EDX) of Au-MWCNTs and PtAu-MWCNTs

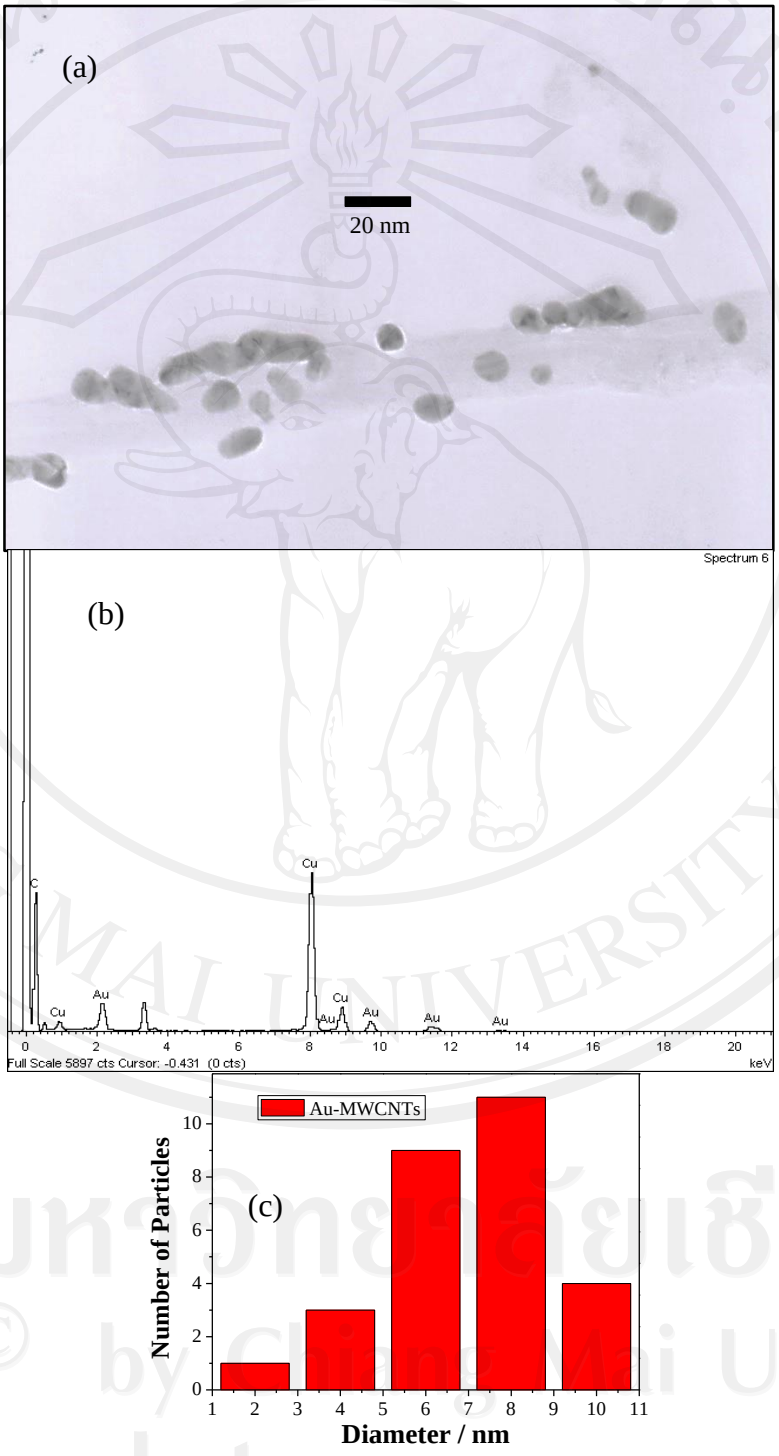


**Figure 3.2** TEM images, EDX spectra and the corresponding particle size distribution histogram of: Au-MWCNTs (a,b,c).

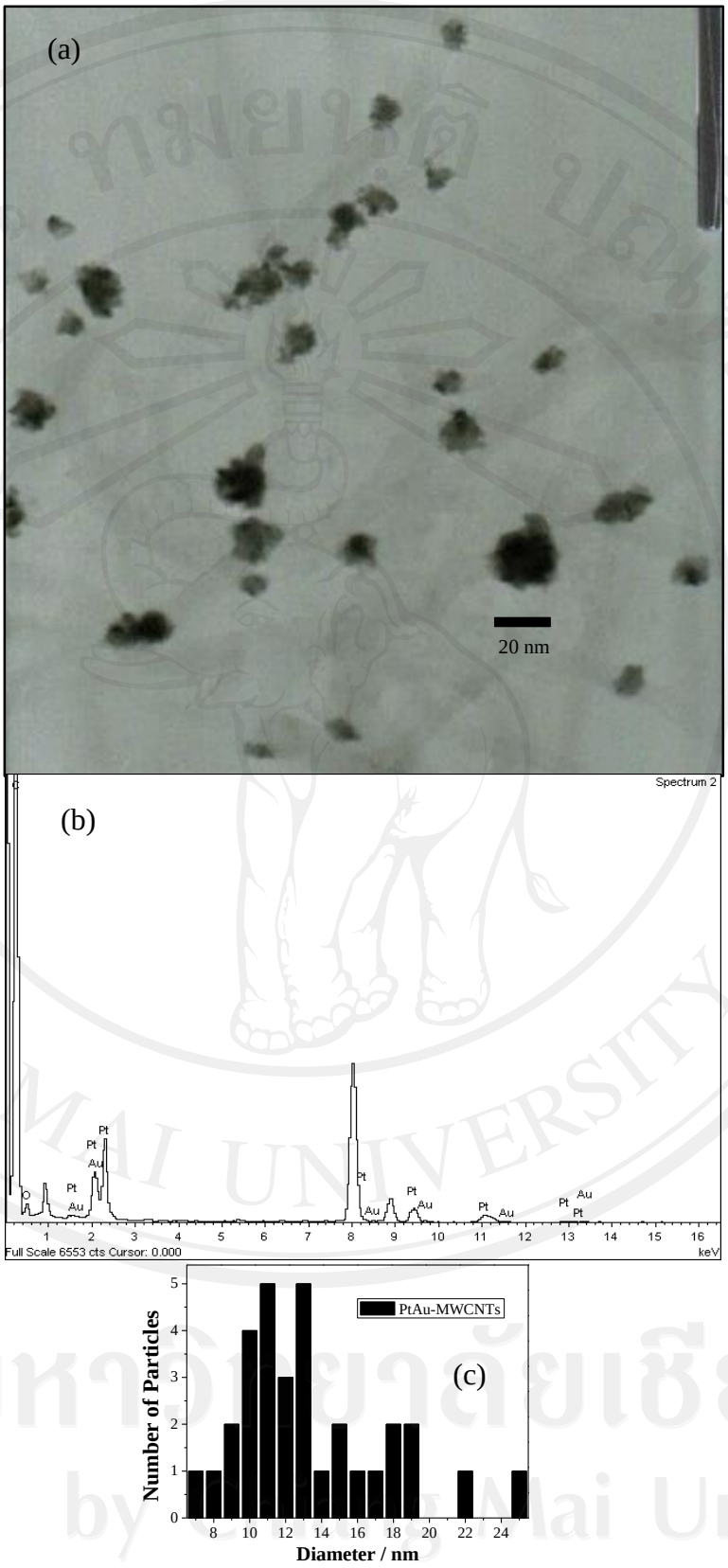


**Figure 3.3** TEM images, EDX spectra and the corresponding particle size distribution histogram of: PtAu-MWCNTs (a,b,c).

Figure 3.2 and 3.3 shows representative TEM topographic images, EDX spectra and particle size distribution histograms of Au-MWCNTs before and after Pt deposition PtAu-MWCNTs, respectively. From the images, the round Au nanoparticles adsorb on MWCNTs with the average particle size of 7.0 ± 2.0 nm while the adsorption of PtAu nanoaparticles on MWCNTs is rougher than those of monometallic Au nanoparticles with the average particle size of 12.8 ± 4.1 nm. Chemical composition analysis by using EDX indicates the presence of Pt on the PtAu catalyst. Anevidence of Cu content in the EDX spectra is attributed to the copper grid which is generally used for sample preparation of EDX analysis.

**3.3 Electrochemical and electrocatalytic characteristics of the electrooxidation of small organic molecules on Au-MWCNTs, Pt-MWCNTs and PtAu-MWCNTs electrodes**

Voltammetric characterization of metal nanoparticles in Figure 3.4(a) shows cyclic voltammograms of MWCNTs, Au-MWCNTs, Pt-MWCNTs and PtAu-MWCNTs electrodes in 1 M $H_2SO_4$ at a potential scan rate of 50 mV $s^{-1}$. In the process of catalyst synthesis, Au and Pt nanoparticles were deposited on functionalized MWCNTs surface by using THPC reducing reagent and electrodeposition, consecutively. PtAu-MWCNTs was synthesized by electrodeposite Pt from $H_2PtCl_6$ solution onto Au-MWCNTs surface. In the cyclic voltammograms, Au-MWCNTs shows no voltammetric characteristic as the blocking effect of the particle hydrophobic protecting layers provide the inaccessible surface by electrolytes in solution. However, voltammetric characteristics become visible for Pt-MWCNTs and PtAu-MWCNTs. The hydrogen desorption peaks imply electro-chemically active

surface area of PtAu-MWCNTs higher than Pt-MWCNTs. This indicates that PtAu-MWCNTs has a different stoichiometry for hydrogen adsorption. However, the voltammograms for MWCNTs and Pt-MWCNTs have a thick double layer. The electro-adsorption of two different hydrogen species are the under-potential and over-potential adsorbed hydrogen ($H_{UPD}$ and $H_{OPD}$) [54]. The electro-adsorption of $H_{UPD}$ is the characteristic of Pt group while the electro-adsorption of $H_{OPD}$ takes place at all electrode materials. As shown in Figure 3.4(a) $H_{UPD}$ in $H_2SO_4$ aqueous electrolyte solution is a phenomenon characteristic of only noble metals. During the positive scan the following potential range can be seen; broad peaks of hydrogen desorption (-0.35 to -0.1 V) followed by the double-layer region (-0.1 to 0.2 V) and oxidation of Pt oxide formation (0.2 to 0.6 V). The reverse processes were occurred during the negative scan.

Cyclic voltammograms of methanol oxidation of Au-MWCNTs, Pt-MWCNTs and PtAu-MWCNTs were measured in a mixture of 2 M $CH_3OH$ and 1 M $H_2SO_4$ as can be seen in Figure 3.4(b). The voltammograms of MWCNTs and Au-MWCNTs show no oxidation peak. Voltammograms of Pt-MWCNTs and PtAu-MWCNTs show a characteristic peak of methanol oxidation that produced a prominent symmetric anodic peak ca. 0.65 V in the forward scan. In the reverse scan, a cathodic peak current density was detected at ca. 0.48 V. In the forward scan, the anodic reaction is incompletely oxidized carbonaceous species to $CO_2$. The carbonaceous species ($COH_{ads}$, $HCO_{ads}$, $HCOO_{ads}$) are also formed during the adsorption phase, and principle by-products are formic acid and formaldehyde [13,26,55]. An appearance of cathodic peak current density at 0.48 V indicates that the re-oxidation of CO and other adsorbed species occurs during the reverse scan [13]. The Pt catalyst surface are

strongly adsorbed by CO and some of the adsorbed species. Therefore, electrocatalytic performance of the Pt-MWCNTs was lower than PtAu-MWCNTs. Au is usually inactive for methanol oxidation but when it was electro-deposited by Pt, it can increase efficiency of electrocatalytic properties of PtAu-MWCNTs.

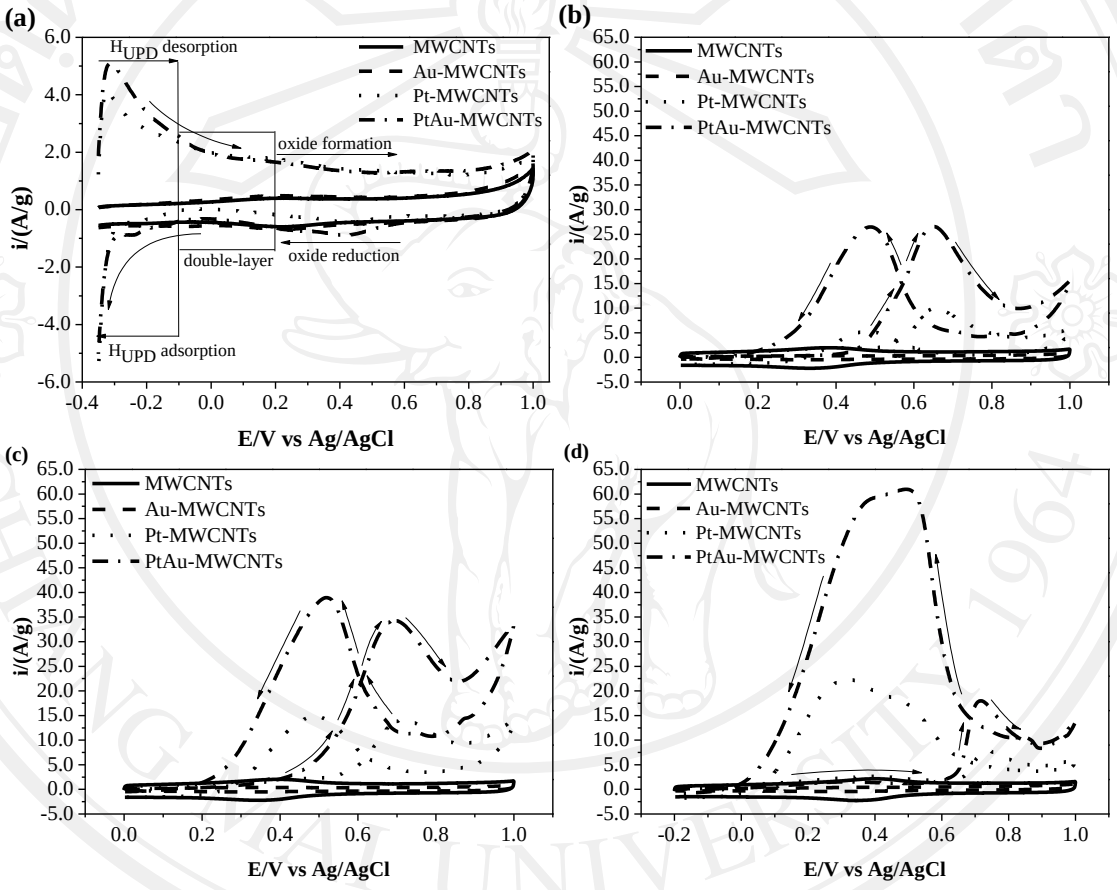


**Figure 3.4** Cyclic voltammograms for electrochemical characterization in (a) 1 M $H_2SO_4$, (b) 2 M $CH_3OH$, (c) $CH_3CH_2OH$ and (d) 2 M HCOOH oxidation of the small organic molecules in 1 M $H_2SO_4$ were monitored when MWCNTs (solid line), Au-MWCNTs (dash line), Pt-MWCNTs (dot line) and Pt/Au-MWCNTs (dash dot line) were used as electrodes. The scan rate was 50 mV $s^{-1}$.

Cyclic voltammograms of ethanol electrooxidation of Au-MWCNTs, Pt-MWCNTs and PtAu-MWCNTs were measured in a mixture of 2 M $CH_3CH_2OH$ and

1 M $H_2SO_4$ shown in Figure 3.4(c). The voltammogram of MWCNTs shows no oxidation peak. Voltammograms of Pt-MWCNTs and PtAu-MWCNTs show a characteristic peak with outstanding oxidation peak in the forward scan and a second oxidation peak at negative potentials in the backward scan [21,23]. The peaks at ca. 0.70 V in anodic scan is attributed to ethanol oxidation and the peak at ca. 0.50 V in the cathodic scan is related to the reaction of the electrode after deactivation giving highest peak to oxidation of unreacted ethanol and absorbed intermediates. The efficiency of the electrocatalyst towards ethanol oxidation is normally characterized by the onset potential of ethanol oxidation and current density of the forward peak. The onset potential and current density of MWCNTs are hardly determined. The onset potentials of Pt-MWCNTs and PtAu-MWCNTs are 0.50 and 0.35 V, respectively. The current densities of Pt-MWCNTs and PtAu-MWCNTs are 12.0 and 35.0 A/g, respectively. PtAu-MWCNTs illustrates more enhancements in current density and lower onset potential than the others.

The activities of MWCNTs, Au-MWCNTs, Pt-MWCNTs, PtAu-MWCNTs electrodes in oxidation of formic acid were studied and compared. Au is used as a second metal in Pt-based alloys to promote the deep oxidation of fuel molecules into $CO_2$. Figure 3.4(d) shows the cyclic voltammograms of the electrodes in a mixture of 2 M HCOOH and 1 M $H_2SO_4$ at a potential scan rate of 50 $mV \cdot s^{-1}$. For Pt-MWCNT, there are two peaks at 0.40 and 0.75 V in anodic scan as the electrooxidation of formic acid follows a dual-pathway mechanism [56,57]. The broad oxidation current peak at potential of ca. 0.30-0.60 V in cathodic sweep is attributed to the formic acid oxidation through the active intermediates. However, the low current density implies

that MWCNTs and Au-MWCNTs are catalytically inefficient in the oxidation of formic acid.

After Pt deposition onto Au-MWCNTs surface providing PtAu-MWCNTs, the electrocatalytic activity develops dramatically. It can be obviously seen that the current density is increase compared to that of the Pt-MWCNTs. In anodic scan, there are also two oxidation peaks observed at 0.35 V and 0.70 V corresponding to the direct oxidation of HCOOH and the oxidation of adsorbed CO and HCOOH, respectively. The potential positions of these two peaks are more negative than that of Pt-MWCNTs electrode. It can be spotted that onset potential shows small cathodic shift of PtAu-MWCNTs indicating that deposition of small Pt amount brought to significant improvement of the catalytic activity in formic acid oxidation.

**3.4 characterization and structure analysis of Pd, Pt and PdPt catalysts loaded functionalized MWCNTs surface**

**3.4.1 Powder X-ray diffraction (XRD)**

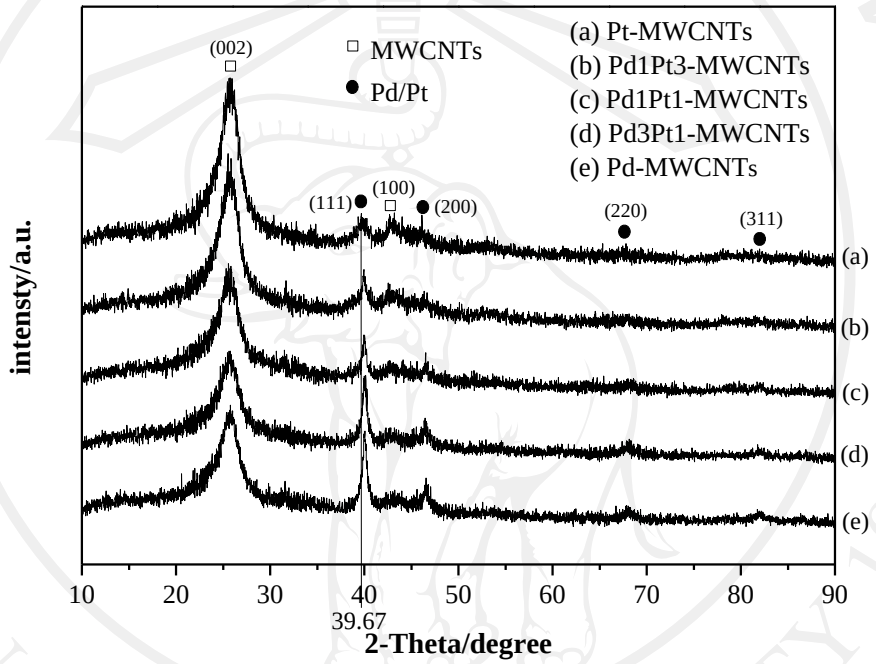


**Figure 3.5** Powder XRD patterns of (a) Pt-MWCNTs, (b) Pd1Pt3-MWCNTs, (c) Pd1Pt1-MWCNTs, (d) Pd3Pt1-MWCNTs and (e) Pd-MWCNTs catalysts.

XRD technique was used to identify the catalyst sample phases**.** X-ray interacts with electrons in sample and a beam of X-rays impinging on an sample will be scattered in various directions by the atomic electrons. The powder XRD patterns of Pt-MWCNTs, Pd1Pt3-MWCNTs, Pd1Pt1-MWCNTs, Pd3Pt1-MWCNTs and Pd-MWCNTs catalysts are shown in Figure 3.5. The strong diffraction peaks at 2-Theta (2θ) values of 26.4º and 42.4º can be assigned to (002) and (100) that are attributed to

hexagonal graphite structure, which suggests MWCNTs has a high graphite structure (JCPDS No. 00-008-0415). The Pd/Pt diffraction peaks show that all catalysts have a face centered cubic (fcc) crystal structure. The diffraction peaks at 2θ values of 39.7º, 46.6º, 67.9º and 81.5º can be assigned to Pt (111), (200), (220) and (311) diffraction peaks, respectively. The isolated Pd/Pt (220) peaks were chosen to calculate the average metal crystalline particle sizes using the Debye-Scherrer formula [58]. The average metal crystalline particle sizes are 10.6, 8.0, 8.7, 9.6 and 7.4 nm for Pt-MWCNTs, Pd1Pt3-MWCNTs, Pd1Pt1-MWCNTs, Pd3Pt1-MWCNTs and Pd-MWCNTs, respectively. Debye-Scherrer formula given by

$$D = \frac{0.9\,\lambda}{\beta\,cos\,\theta} \tag{2.1}$$

where *D* is the apparent particle size, $\beta$ is a full-width half-maximum (FWHM) of the X-ray diffraction line (additional peak broadening) in radians, $\lambda$ is the wavelength used, and $\theta$ is a half the scattering angle. The constant 0.9 in Eq. (2.1) depends slightly on the symmetry of the crystal. By using the THPC and Sodium L-ascorbate reduction methods, the diffraction peaks of the prepared catalysts shift to the right with increasing amount of Pd catalyst. Furthermore, the diffraction peaks shift to the right of 2θ, it was corresponding with Bragg's law equation as in $n\lambda = 2d\sin\theta$. When the diffraction peaks shift to the right, the *d*-spacing are decreasing as shown in Table 3.1. The diffraction peaks was compared with a vertical line at 2θ value of 39.67º in Figure 3.4 which marks the 2θ position of Pt (111) peak (JCPDS No. 00-001-1190). The lattice parameter ($a_0$) can be calculated by using Eq. 2.2.

$$a_0 = d_{hkl}\sqrt{h^2 + k^2 + l^2} \quad (2.2)$$

Where *h*, *k* and *l* are integers, positive and negative or zero, respectively. (*h*,*k*,*l*) are the Miller indices for a particular family of planes. $d_{hkl}$ is d-spacing which is the separation of planes [61].

$a_0$ of the Pt-MWCNTs, Pd1Pt3-MWCNTs, Pd1Pt1-MWCNTs, Pd3Pt1-MWCNTs and Pd-MWCNTs, calculated from the (111) peak are 3.9307, 3.9307, 3.9129, 3.8652 and 3.8604 Å, respectively. $d_{hkl}$ are obtained from Table 3.1. The lattice parameters of carbon supported PdPt catalysts are higher than the value for fcc Pd but smaller than that of for fcc Pt. These indicate the contraction of the lattice due to the substitution of Pt by Pd in the fcc structure or the formation of PdPt alloy [59,60].

### 3.4.2 Transmission electron microscopy (TEM)

Figure 3.6 to 3.10 show the TEM images with the corresponding selected area electron diffraction (SAED) patterns and the corresponding particle size distribution histograms of Pd-MWCNTs, Pt-MWCNTs, Pd3Pt1-MWCNTs, Pd1Pt1-MWCNTs and Pd1Pt3-MWCNTs obtained from THPC and sodium L-ascorbate reduction methods. It can be seen from Figure 3.10 that the smallest Pd1Pt3 particle sizes are uniformly dispersed on the MWCNTs surface, while the dispersion of Pt and Pd3Pt1 particles on the MWCNTs surface is uneven with large agglomeration. The average particle size for Pd-MWCNTs, Pt-MWCNTs, Pd3Pt1-MWCNTs, Pd1Pt1-MWCNTs and Pd1Pt3-MWCNTs are 3.9 ± 0.9, 9.8 ± 1.8, 18.8 ± 3.8, 3.2 ± 1.4 and 3.0 ± 0.6 nm, respectively. The sizes of Pt-MWCNTs and Pd3Pt1-MWCNTs are larger, while the

Pd-MWCNTs, Pd1Pt1-MWCNTs and Pd1Pt3-MWCNTs are smaller than the values calculated from XRD patterns. The SAED patterns on the nanoparticles are shown in Figure 3.6 to 3.10. The black rings with occasional black spots signify the crystalline nature of the nanoparticles. Figure 3.6 shows that the diffracted ring patterns of (002) of MWCNTs and (111), (200), (220), (311) and (420) planes of Pd were identified. Figure 3.7 shows the diffracted ring patterns of (002) and (101) of MWCNTs and (111), (200), (220), (311) and (420) planes of Pt. Figure 3.8 to 3.10 shows the similar diffracted ring patterns of (002), (101) and (004) of MWCNTs and (111), (200), (220), (311) and (222) planes of PdPt fcc crystal structure. The SAED results can support XRD results that Pt nanoparticles are substituted by Pd nanoparticles in the fcc structure, *d*-spacing of (111) and (200) planes of catalysts decrease with increasing amount of Pd catalyst as shown in Table 3.1.

**Table 3.1** *d*-spacing of (111) and (200) planes of catalysts.

| **Catalysts** | ***d*-spacing** | |
|---|---|---|
| | **(hkl) (111)** | **(hkl) (200)** |
| Pt-MWCNTs | 2.2694 | 2.0131 |
| Pd1Pt3-MWCNTs | 2.2694 | 2.0131 |
| Pd1Pt1-MWCNTs | 2.2591 | 1.9812 |
| Pd3Pt1-MWCNTs | 2.2489 | 1.9656 |
| Pd-MWCNTs | 2.2288 | 1.9351 |

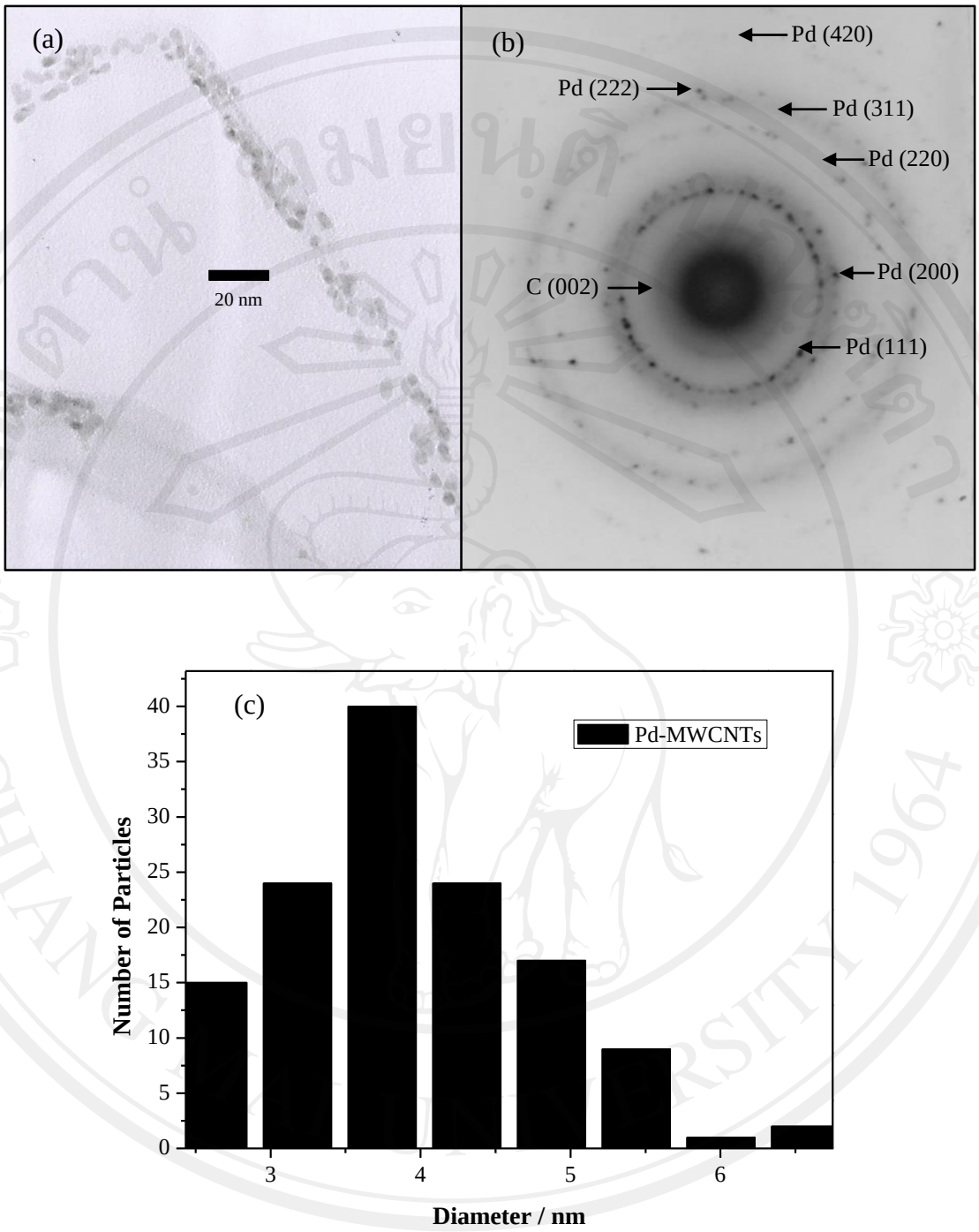


**Figure 3.6** TEM images (a) with the corresponding SAED patterns (b) and the corresponding particle size distribution histogram (c) of Pd-MWCNTs.

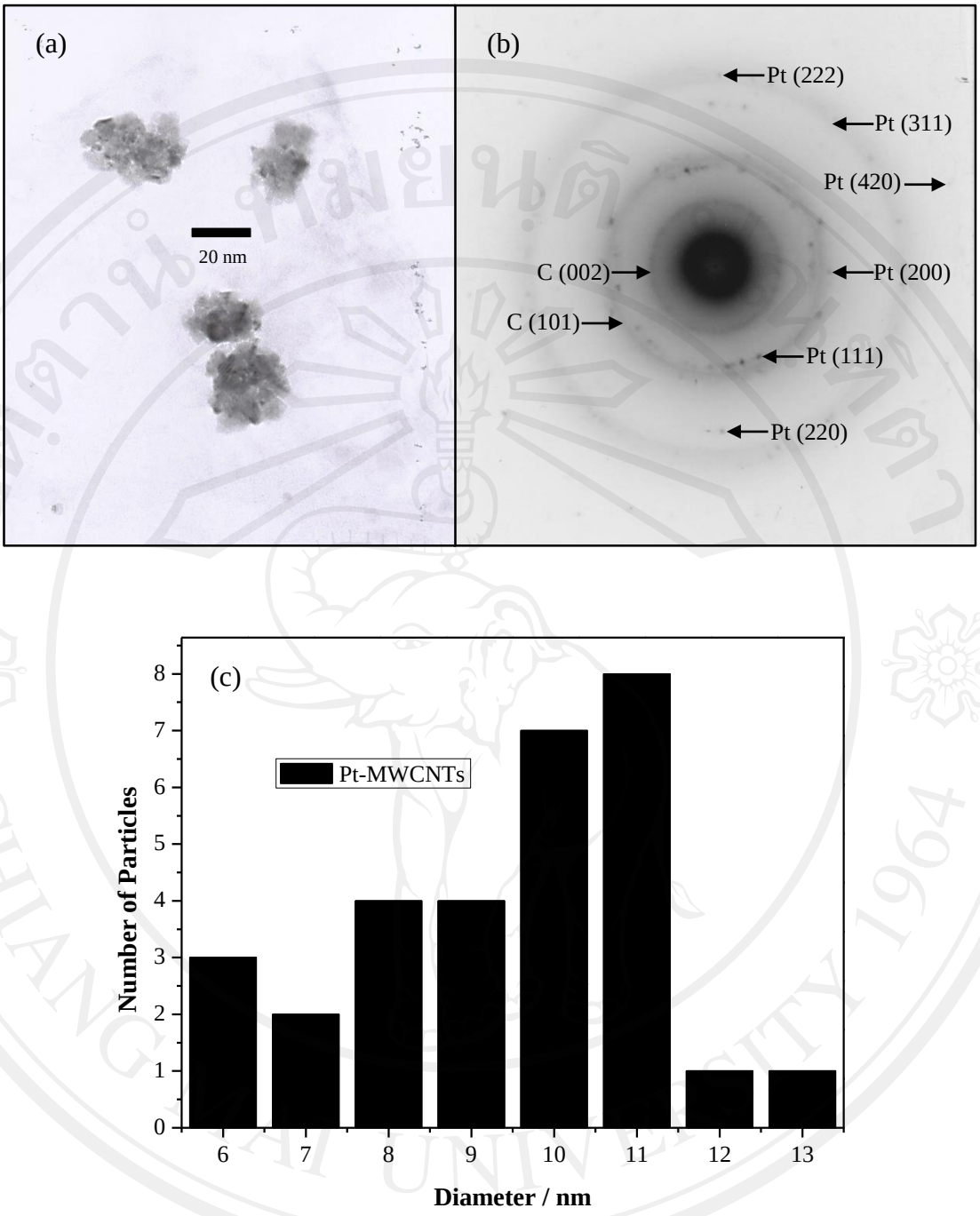


**Figure 3.7** TEM images (a) with the corresponding SAED patterns (b) and the corresponding particle size distribution histogram (c) of Pt-MWCNTs.

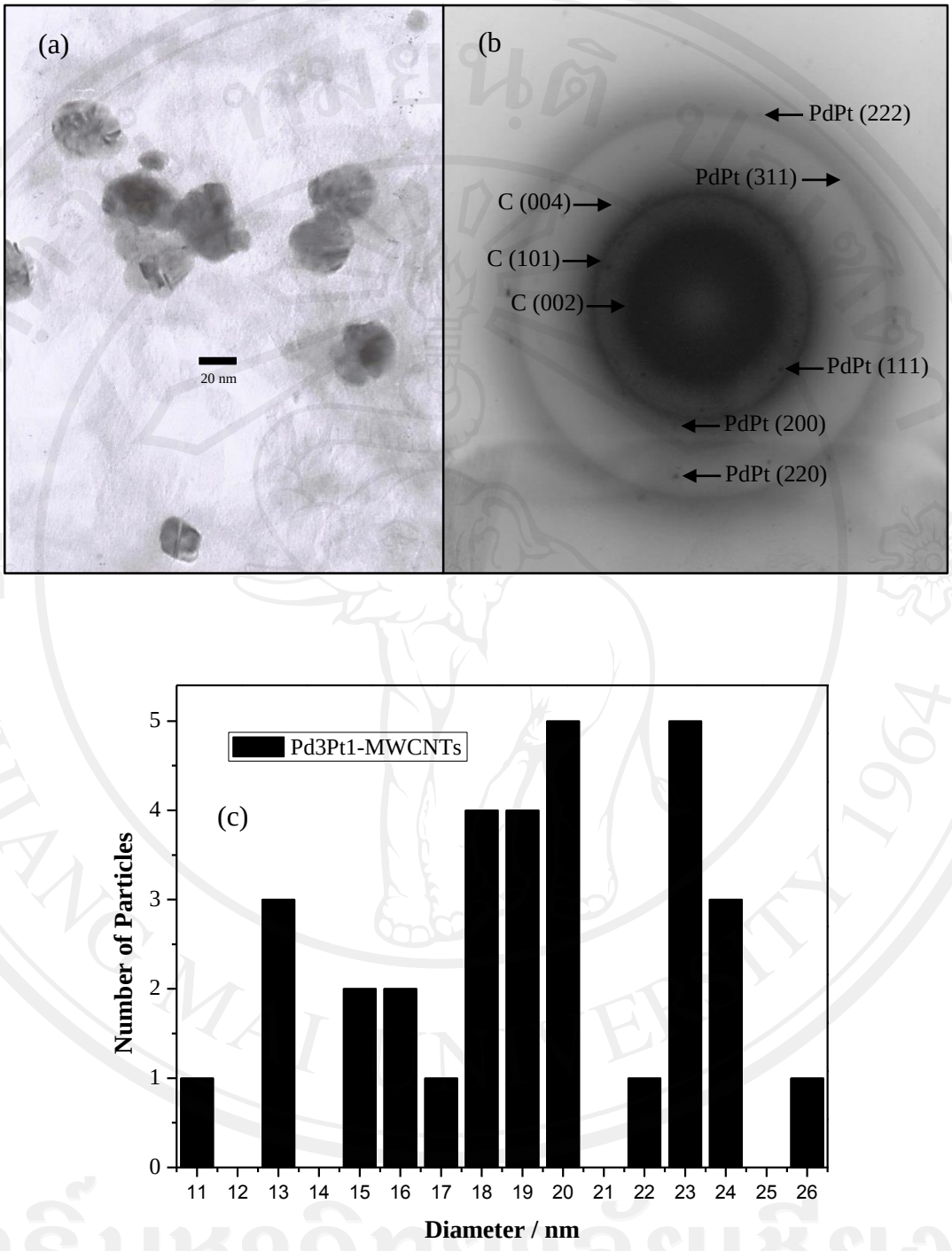


**Figure 3.8** TEM images (a) with the corresponding SAED patterns (b) and the corresponding particle size distribution histogram (c) of Pd3Pt1-MWCNTs.

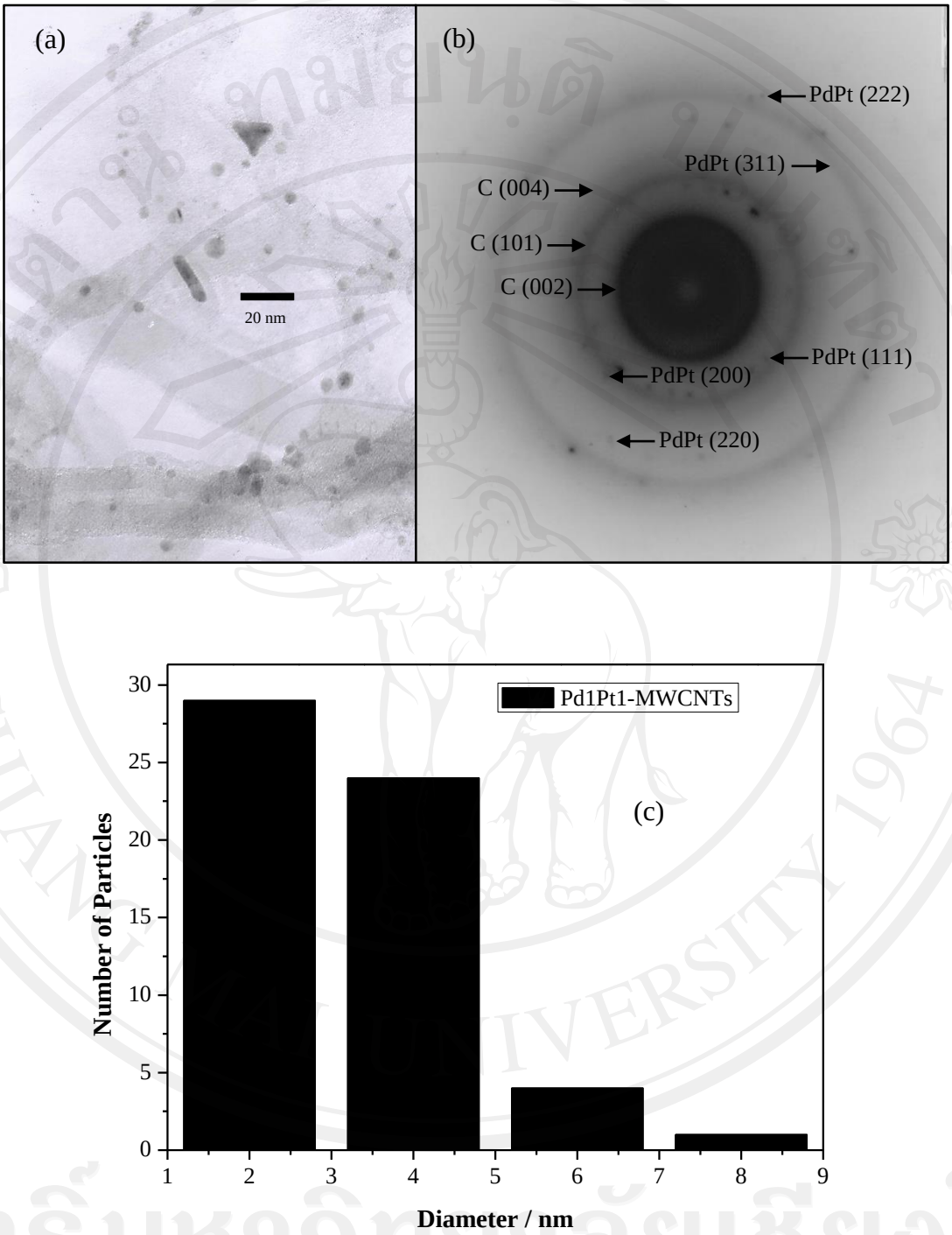


**Figure 3.9** TEM images (a) with the corresponding SAED patterns (b) and the corresponding particle size distribution histogram (c) of Pd1Pt1-MWCNTs.

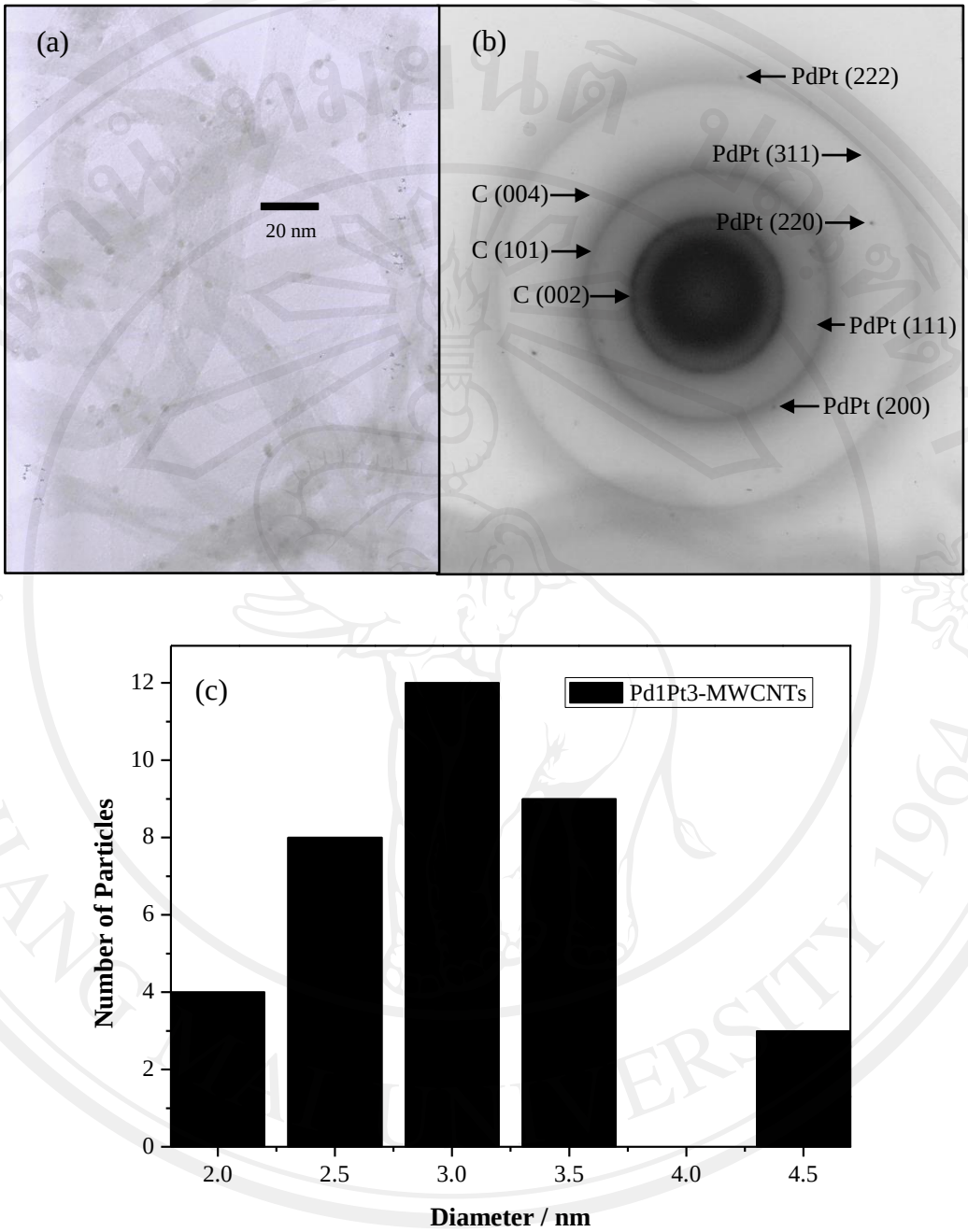


**Figure 3.10** TEM images (a) with the corresponding SAED patterns (b) and the corresponding particle size distribution histogram (c) of Pd1Pt3-MWCNTs.

## 3.5 Electrochemical and electrocatalytic characteristics of the electro-oxidation of small organic molecules on Pd-MWCNTs, Pt-MWCNTs and PdPt-MWCNTs electrodes

### 3.5.1 Electrochemical characterization of PdPt-MWCNTs-Nafion nano-composite-modified glassy carbon electrode

To investigate the electrochemical properties of the MWCNTs, Pd-MWCNTs, Pt-MWCNTs, Pd3Pt1-MWCNTs, Pd1Pt1-MWCNTs and Pd1Pt3-MWCNTs-Nafion film-modified glassy carbon electrodes, cyclic voltammetry in 1.0 M $H_2SO_4$ solution at a scan rate of 50 mV $s^{-1}$ were performed. Figure 3.11 shows the different regions from 1 to 5 which describe different processes occurring at the surface of the catalysts. The region 1 extending from -0.35 to 0.03 V vs Ag/AgCl represents the hydrogen desorption ($H_{des}$) from the surface of metal catalysts. The hydrogen desorption exhibits a few pairs of well-defined peaks due to the presence of different Pd or Pt crystalline facets. The region 2 extending from 0.03 to 0.18 V vs Ag/AgCl shows double layer charging and discharging. The reactions which occur at region 3 are the formation of oxygen on the surface of metal catalysts. Metals catalyze water dissociation obtaining oxide species. Then, metals surface was covered with an oxide layer. Beyond region 3, the oxygen gas evolution starts to dominate so a reverse scan would immediately perform. When the scan direction was reversed, the reduction of oxide layer was shown in region 4. During the cathodic scan from 0.03 V down, the underpotential deposition of hydrogen atom occurs from the reduction of protons. The hydrogen adsorption ($H_{ads}$) exhibits a few pairs of well-defined peaks for different Pd or Pt facets, which is similar to hydrogen desorption [19].

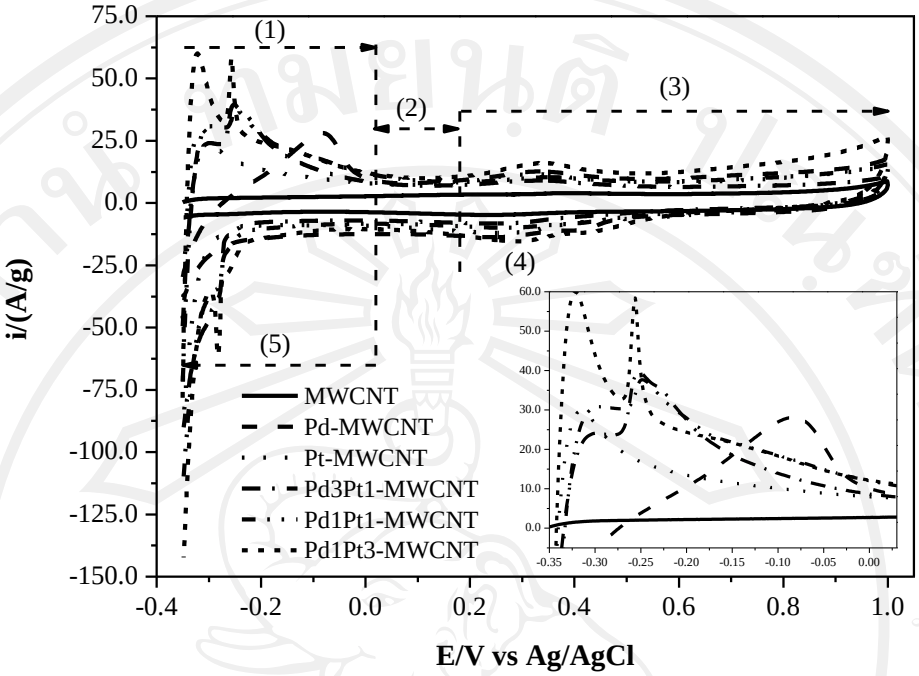


**Figure 3.11** Cyclic voltammograms recorded in 1 M $H_2SO_4$ solution for MWCNTs (solid line), Pd-MWCNTs (dash line), Pt-MWCNTs (dot line), Pd3Pt1-MWCNTs (dash dot line), Pd1Pt1-MWCNTs (dash dot dot line) and Pd1Pt3-MWCNTs (short dash) electrodes in the potential range of -0.35 to 1.00 V with scan rate of 50 $mV \cdot s^{-1}$.

As shown in the inset of Figure 3.11, hydrogen desorption and hydrogen adsorption can be observed in this voltage range, no hydrogen desorption and no adsorption peak appeare, when cyclic voltammetry was carried out with the MWCNTs-Nafion film-modified glassy carbon electrode. Hydrogen desorption peak potentials of the alloy catalysts negatively shift from -0.08 to -0.26 V vs Ag/AgCl when amount of Pd decreases. On the other hand, hydrogen desorption peak potentials positively shift from -0.31 to -0.30 V vs Ag/AgCl when amount of Pt decrease. The hydrogen desorption and hydrogen adsorption peaks at relatively negative potentials may be described to hydrogen species in and out of the metals lattice interstices

accompanied by hydrogen electrooxidation and hydrogen electroreduction on metals surfaces in the positive and negative scans, respectively [62].

**3.5.2 Electrocatalytic activity for small organic molecules electrooxidation at the PdPt–MWCNTs-Nafion nanocomposite-modified glassy carbon electrode**

Cyclic voltammograms of methanol oxidation of Pd-MWCNTs, Pt-MWCNTs and PdPt-MWCNTs were measured in 2 M $CH_3OH$ in 1 M $H_2SO_4$ solution in Figure 3.12 (a and b). The voltammogram of MWCNTs shows no oxidation peak which Pd-MWCNTs observe a small anodic peak at 0.37 V. Voltammograms of Pt-MWCNTs, Pd1Pt3-MWCNTs, Pd1Pt1-MWCNTs and Pd1Pt3-MWCNTs show a characteristic peak of methanol oxidation that produced a prominent symmetric anodic peak ca. 0.60 V in the forward scan. In the reverse scan, a cathodic peak current density was detected at ca. 0.40 V. In the forward scan, the anodic reaction is incompletely oxidized carbonaceous species formed into $CO_2$. The carbonaceous species are also formed during the adsorption phase, $COH_{ads}$, $HCO_{ads}$, $HCOO_{ads}$, and principle by-products are formic acid and formaldehyde [13,26,55]. A cathodic peak current density at 0.40 V, the re-oxidation of CO and other adsorbed species occurs during the reverse scan [13]. Voltammograms of Pd1Pt3-MWCNTs were higher than the others. Moreover, it was obvious that the current densities of both anodic peak and cathodic peak were negatively shifted, an anodic peak current density was detected at 0.58 V and a cathodic peak current density was detected at 0.37 V. The result indicates that Pd1Pt3-MWCNTs revealed better performance for the methanol oxidation than the others. These results can be ascribed to the large number of active oxygen-containing species, such as PdO and PdOx formed in the course of the methanol oxidation and

could address the problem of Pt catalyst poisoning by CO-like species. The Pd catalysts help significantly improve the oxidative removal of CO on the Pt catalyst suface by making available several active oxygen-containing species such as PdO and $PdO_x$ [63,64]. Therefore, it can increase efficiency of electrocatalytic properties of Pd1Pt3-MWCNTs.

Cyclic voltammograms of ethanol oxidation of Pd-MWCNTs, Pt-MWCNTs and PdPt-MWCNTs were measured in 2 M $CH_3CH_2OH$ in 1 M $H_2SO_4$ solution in Figure 3.12(c and d). The voltammogram of MWCNTs shows no oxidation peak. Voltammograms of Pd-MWCNTs obtain a few two oxidation peaks at ca. 0.40 V. The voltammograms of Pd1Pt3-MWCNTs show a characteristic peak with oxidation peaks in the forward scan and outstanding second oxidation peaks at negative potentials in the backward scan. The peaks at ca. 0.65 V in anodic scan is attributed to ethanol oxidation. During the cathodic scan, there is a steep increase of the current at ca. 0.58 V, followed by a higher current peak at ca. 0.38 V, due to ethanol oxidation of the electrode after deactivation giving highest peak to oxidation of unreacted ethanol and absorbed intermediates (e.g. CO, $CH_3CO$, $CH_3CHO$, $CH_3COOH$ and $CO_2$) [13]. The efficiency of the electrocatalyst towards ethanol oxidation is normally characterized by the onset potential of ethanol oxidation and current density of the forward peak. The onset potential and current density of MWCNTs are hardly determined. The onset potentials of Pt-MWCNTs, Pd3Pt1-MWCNTs, Pd1Pt1-MWCNTs and Pd1Pt3-MWCNTs are 0.50, 0.52, 0.48 and 0.46 V, respectively. Pd1Pt3-MWCNTs illustrate more enhancements in current density and the onset potential is shifted to more negative potentials than the others.

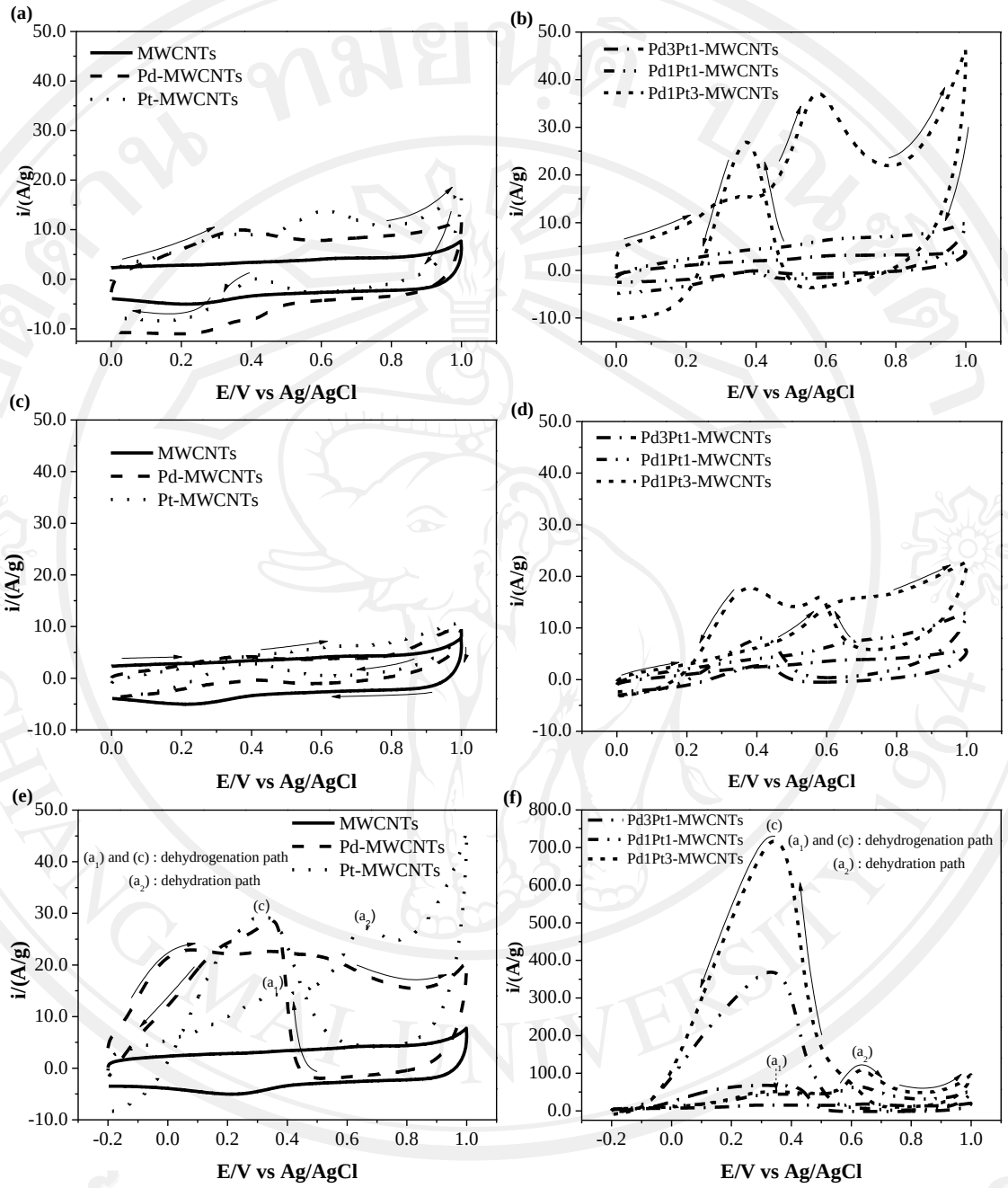


**Figure 3.12** Cyclic voltammograms for oxidation of small organic molecules in 1 M $H_2SO_4$ at MWCNTs (solid line), Pd-MWCNTs (dash line), Pt-MWCNTs (dot line), Pd3Pt1-MWCNTs (dash dot line), Pd1Pt1-MWCNTs (dash dot dot line) and Pd1Pt3-MWCNTs (short dash line). (a and b) 2 M $CH_3OH$, (c and d) $CH_3CH_2OH$ and (e and f) 2 M HCOOH, scan rate of 50 $mV \cdot s^{-1}$.

Figure 3.12 (e and f) shows the cyclic voltammograms for MWCNTs, Pd-MWCNTs, Pt-MWCNTs, Pd3Pt1-MWCNTs, Pd1Pt1-MWCNTs and Pd1Pt3-MWCNTs in 2 M HCOOH in 1 M $H_2SO_4$ solution at the potential range -0.20 to 1.00 V vs Ag/AgCl with a scan rate of 50 $mV \cdot s^{-1}$. Figure 3.11 (e) shows both positive scan and negative scan at MWCNTs are not shown the formic acid oxidation. Two peaks are observed in the positive scan at anodic peak ($a_1$) and the negative scan at cathodic peak (c) for Pd-MWCNTs, indicating that the oxidation of formic acid to $CO_2$ on Pd-MWCNTs follows the direct path or dehydrogenation path. The anodic peak ($a_1$) of Pt-MWCNTs is less than Pd-MWCNTs due to Pt sites are not blocked by the poisoning $CO_{ads}$ [65,66]. The dehydrogenation path (Reaction (1.13)) is preferred since formic acid is directly oxidized to form $CO_2$ without forming $CO_{ads}$ intermediates.

In contrast, the cyclic voltammograms for Pt-MWCNTs, Pd3Pt1-MWCNTs, Pd1Pt1-MWCNTs and Pd1Pt3-MWCNTs are obtained two peaks in the positive scan at anodic peak ($a_1$) and anodic peak ($a_2$), and one peak in the negative scan at cathodic peak (c). The first small anodic peak ($a_1$) is due to the direct oxidation of formic acid to $CO_2$ on the remaining sites unblocked by intermediate $CO_{ads}$. The second anodic peak ($a_2$) is related to the oxidation of $CO_{ads}$ follows the indirect path or dehydration path (Reaction (1.16)), which releases the surface sites for the subsequent direct oxidation of formic acid. On the negative scan, a large cathodic peak (c) is observed, as most of the surface sites are free from occupation by the $CO_{ads}$ and oxide species and thus available for the formic acid oxidation.

The cyclic voltmmogram for Pd-based binary with Pt catalysts supported on MWCNTs indicate quite different behavior. Figure 3.12 (f) shows that the onset potential for the reaction on Pd1Pt3-MWCNTs is about -0.17 V. The current density raises up to 51.18 A/g at 0.34 V and reaches a peak higher than the other catalyst-MWCNTs. Among PdPt catalysts Pd1Pt3-MWCNTs is the best for indirect formic acid oxidations at anodic peak ($a_2$) with the current density raising up to 107.94 A/g at 0.63 V. At higher potentials, formic acid oxidation is deactivated as a result of Pt surface oxidation. In the negative scan, the surface remains inactive, until partial reduction of the irreversibly formed Pt surface oxides takes place, and further current increase is due to the formic acid oxidation on the catalyst surface free from occupation by the $CO_{ads}$ in dehydrogenation path at cathodic peak (c), which current density raises up to 716.89 $A/g_{metals}$ at 0.34 V. All oxidation peaks on these catalysts are higher than the others, indicating that formic acid oxidation is facilitated on the Pd-containing Pt catalysts.

### 3.5.3 The activity and stability of anodic catalysts PdPt–MWCNTs-Nafion nanocomposite-modified glassy carbon electrode

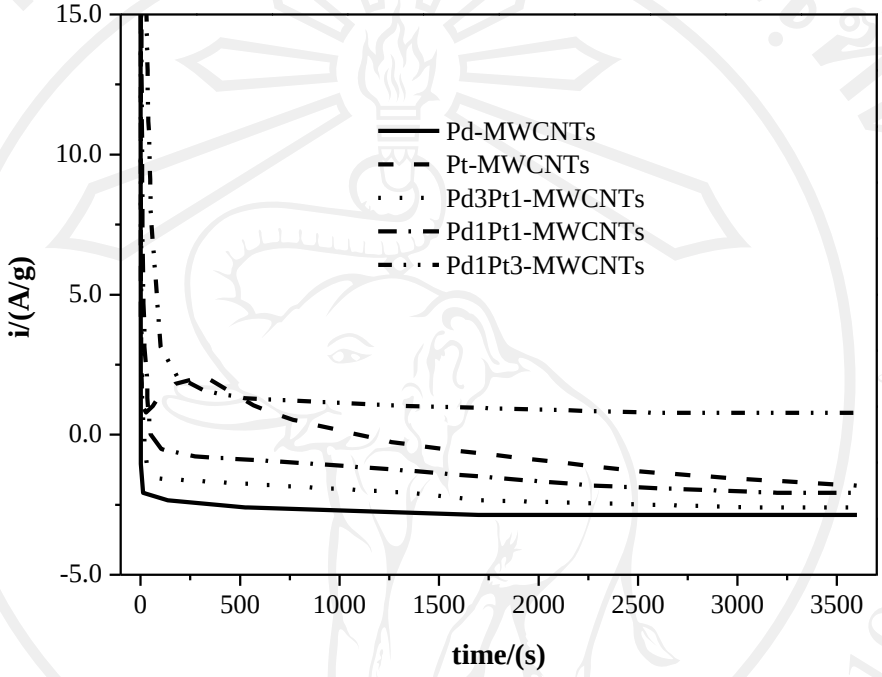


**Figure 3.13** Amperometric current density - time curves of Pd-MWCNTs (solid line), Pt-MWCNTs (dash line), Pd3Pt1-MWCNTs (dot line), Pd1Pt1-MWCNTs (dash dot line) and Pd1Pt3-MWCNTs (dash dot dot line) in 2 M HCOOH in 1 M $H_2SO_4$ solution at 0.30 V vs Ag/AgCl for 3,600 second reaction time.

Amperometric current density - time curves of Pd-based binary with Pt catalysts supported on MWCNTs surface are presented in Figure 3.13. The curves clearly show the decay of the densities with time, especially in the beginning and at the constant potential of 0.30 V for 3,600 s. In the current of Pt-MWCNTs catalysts was rapidly decreased in the initial period of the experiments, following by a slow decreased. A possible reason about the slow decrease of current density is the poisoning effect by $CO_{ads}$ intermediates in the dehydration path [67]. Formic acid

oxidation current at the Pd-MWCNTs catalysts rapidly decreased in the initial period of the experiments, suggesting that all catalysts are easily poisoned. Furthermore, the amperometric current density - time curves are observed and formic acid oxidation current density at the Pd-MWCNTs, Pt-MWCNTs, Pd3Pt1-MWCNTs, Pd1Pt1-MWCNTs and Pd1Pt3-MWCNTs catalyst electrodes at 3,600 s are -2.86, -1.82, -2.61, -2.08 and 0.78 A/g, respectively. The higher current density (0.78 A/g at 3,600 s) indicates the superior activity and stability for formic acid oxidation on the Pd1Pt3-MWCNTs, which is consistent with the result of cyclic voltammetry.

**3.5.4 Electrocatalytic activity for formic acid electrooxidation at the PdPt–MWCNTs-Nafion nanocomposite-modified glassy carbon electrode after amperometry i – t experiments**

Figure 3.14 shows the cyclic voltammograms for MWCNTs, Pd-MWCNTs, Pt-MWCNTs, Pd3Pt1-MWCNTs, Pd1Pt1-MWCNTs and Pd1Pt3-MWCNTs in 2 M HCOOH in 1 M $H_2SO_4$ solution after amperometric i – t experiments at the potential range -0.20 to 1.00 V vs Ag/AgCl with a scan rate of 50 $mV \cdot s^{-1}$. In comparison with the cyclic voltammetry result before and after amperometric i – t experiments, the value of current density at anodic peak ($a_1$), anodic peak ($a_2$) and cathodic peak (c) after amperometric i – t experiments had decreased shown in Table 3.2, 3.3 and 3.4. The results of dehydrogenation path at anodic peak ($a_1$) for the formic acid oxidation at catalysts-MWCNTs before and after amperometric i – t experiments were shown in Table 3.2. It is obvious that the current densities of both before and after amperometric i – t experiments of Pd1Pt3-MWCNTs are highest with 32.96 % current density loss. However, it loses less than Pd-MWCNTs (loss 42.49 %) and the

potential shift to positive potential (0.34 to 0.36 V) 5.88 %. This can be due to the stability decrease and some active sites occupied by $CO_{ads}$ intermediate species during the dehydrogenation path of formic acid oxidation. The dehydration path at anodic peak ($a_2$) for formic acid oxidation at catalysts-MWCNTs before and after amperometric i – t experiments were shown in Table 3.3. It can be observed that the 31.77 % Pd1Pt3-MWCNTs shows highest electroactivity with current density loss. A possible reason about the loss of current density is the $CO_{ads}$ intermediate species occurred during the dehydration path [68,69]. This indicates that the incorporation of Pd with Pt nanoparticles of Pd1Pt3-MWCNTs greatly enhanced the dehydration path of formic acid oxidation. On the other hand, Pd nanoparticles of Pd1Pt3-MWCNTs reduced the $CO_{ads}$ intermediate species. As shown in Table 3.3, Pd-MWCNTs has no peak corresponds to dehydration path of formic acid oxidation. In this case, Pd is a metal known for its ability to catalyse the oxidation of $CO_{ads}$. Furthermore, Pd does not likely act as an OH source because they are not required for dehydration path of formic acid oxidation [26]. In the negative scan, the surface catalysts can completely react with formic acid molecules by free from occupied by $CO_{ads}$. Both before and after amperometric i - t experiments of the Pd1Pt3-MWCNTs show the highest current density and the current density loses only 28.52 % compared with others as shown in Table 3.4. This indicates that the incorporation of Pd with Pt nanoparticles of Pd1Pt3-MWCNTs prepared by THPC and sodium L-ascorbate reduction methods, were the best stability and electroactivity for the formic acid oxidation.

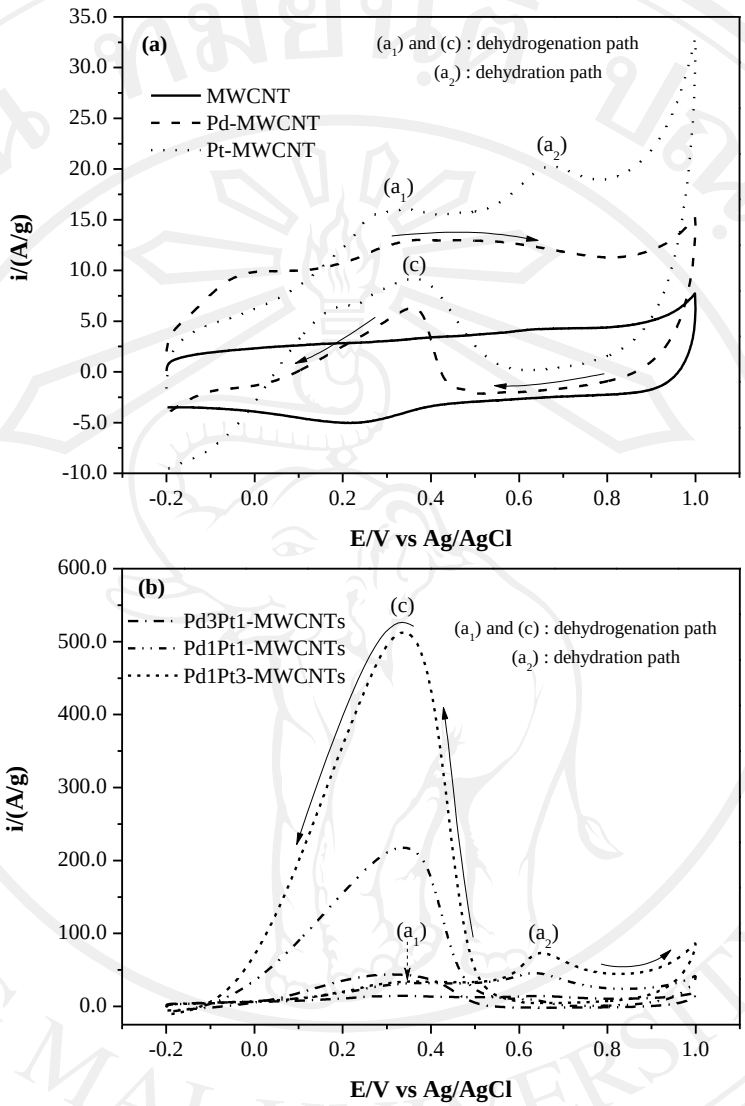


**Figure 3.14** (a) Cyclic voltammograms of MWCNTs (solid line), Pd-MWCNTs (dash line), Pt-MWCNTs (dot line), and (b) Cyclic voltammograms of Pd3Pt1-MWCNTs (dash dot line), Pd1Pt1-MWCNTs (dash dot dot line) and Pd1Pt3-MWCNTs (short dash line) were recorded in 2 M HCOOH in 1 M $H_2SO_4$ solution after chrono-amperometry experiment at the potential range -0.20 to 1.00 V vs Ag/AgCl with a scan rate of 50 $mV \cdot s^{-1}$.

**Table 3.2** Dehydrogenation path ($a_1$) for the formic acid oxidation at catalysts-MWCNTs before and after amperometric i – t experiments**.**

| Catalysts | Anodic peak (dehydrogenation path ($a_1$)) for the formic acid oxidation | | | | | |
|---|---|---|---|---|---|---|
| | Before | | After | | % Changing | |
| | $E_{pa}$ (V vs Ag/AgCl) | $I_{pa}$ (A/g) | $E_{pa}$ (V vs Ag/AgCl) | $I_{Pa}$ (A/g) | $E_{pa}$ (V vs Ag/AgCl) | $I_{pa}$ (A/g) |
| Pd-MWCNTs | 0.35 | 22.64 | 0.37 | 13.02 | 5.71 | -42.49 |
| Pt-MWCNTs | 0.36 | 14.24 | 0.35 | 16.02 | -2.78 | 12.50 |
| Pd3Pt1-MWCNTs | 0.34 | 15.41 | 0.34 | 14.48 | - | -6.04 |
| Pd1Pt1-MWCNTs | 0.36 | 44.49 | 0.37 | 32.12 | 2.78 | -27.80 |
| Pd1Pt3-MWCNTs | 0.34 | 51.18 | 0.36 | 34.31 | 5.88 | -32.96 |

**Table 3.3** Dehydration path ($a_2$) for the formic acid oxidation at catalysts-MWCNTs before and after amperometric i – t experiments**.**

| Catalysts | Anodic peak (dehydration path ($a_2$)) for the formic acid oxidation | | | | | |
|---|---|---|---|---|---|---|
| | Before | | After | | % Changing | |
| | $E_{pa}$ (V vs Ag/AgCl) | $I_{pa}$ (A/g) | $E_{pa}$ (V vs Ag/AgCl) | $I_{Pa}$ (A/g) | $E_{pa}$ (V vs Ag/AgCl) | $I_{pa}$ (A/g) |
| Pd-MWCNTs | - | - | - | - | - | - |
| Pt-MWCNTs | 0.66 | 27.09 | 0.67 | 20.25 | 1.51 | -25.25 |
| Pd3Pt1-MWCNTs | 0.64 | 17.97 | 0.64 | 12.72 | - | -29.22 |
| Pd1Pt1-MWCNTs | 0.62 | 64.21 | 0.64 | 45.71 | 3.22 | -28.81 |
| Pd1Pt3-MWCNTs | 0.63 | 107.94 | 0.65 | 73.20 | 3.17 | -31.77 |

**Table 3.4** Dehydrogenation path (c) for the formic acid oxidation at catalysts-MWCNTs before and after amperometric i – t experiments.

| Catalysts | Cathodic peak (dehydrogenation path (c)) for the formic acid oxidation | | | | | |
|---|---|---|---|---|---|---|
| | Before | | After | | % Changing | |
| | $E_{pa}$ (V vs Ag/AgCl) | $I_{pa}$ (A/g) | $E_{pa}$ (V vs Ag/AgCl) | $I_{Pa}$ (A/g) | $E_{pa}$ (V vs Ag/AgCl) | $I_{pa}$ (A/g) |
| Pd-MWCNTs | 0.34 | 28.63 | 0.36 | 6.30 | 5.88 | -78.00 |
| Pt-MWCNTs | 0.32 | 29.40 | 0.36 | 9.20 | 12.50 | -68.71 |
| Pd3Pt1-MWCNTs | 0.32 | 67.76 | 0.32 | 32.31 | - | -52.32 |
| Pd1Pt1-MWCNTs | 0.33 | 368.66 | 0.34 | 217.60 | 3.03 | -40.98 |
| Pd1Pt3-MWCNTs | 0.34 | 716.89 | 0.34 | 512.39 | - | -28.52 |